Tuning water-responsiveness with Bombyx mori silk–silica nanoparticle composites

COMMUNICATION

Tuning water-responsiveness with *Bombyx mori* silk-silica nanoparticle composites

Yeojin Jung[a,b], Samaneh Sharifi Golru[a,c], Tai-De Li[b,d], Elizabeth J. Biddinger[a,c], Raymond S. Tu[a,b*], and Xi Chen[a,b,c,e*]

***Bombyx (B.) mori* silk's water-responsive actuation correlates to its high β-sheet crystallinity. In this research, we demonstrated that stiff silica nanoparticles can mimic the role of dispersed β-sheet nanocrystals and dramatically increase amorphous silk's water-responsive actuation energy density to ~ 700 kJ m^{-3}.**

Water-responsive (WR) materials can reversibly swell and shrink in response to humidity changes, converting the chemical potential of water into mechanical energy[1]. Such WR materials have recently shown great potential as powerful and efficient actuators for broad engineering applications, including robotics[2], shape morphing[3], and smart structures[4]. Nature has developed a number of WR structure/material examples, such as pine cones[5], wheat awns[6], microbes[7], and spider silk[8]. Spider dragline silk can generate WR cyclic stress of 80 MPa, and its WR energy density can reach ~500 kJ m^{-3}, which is significantly higher than those of most known natural muscles[8,9]. While the fundamental mechanisms of the high-energy WR actuation of natural WR materials remains understudied, most cellulose- and protein-based materials share similarities in their structures. The common feature connecting these materials is nanoscale and stiff crystalline regions dispersed in soft hygroscopic amorphous regions[10,11]. Our recent studies showed that *B. mori* silk's WR actuation correlate to the fraction of β-sheet crystalline domains[9]. We noted that, while *B. mori* silk's β-sheet nanocrystals do not contribute to any water adsorption, increasing in silk's crystallinity from 19.7% to 57.6% can dramatically increase the whole structure's WR energy density from ~200 kJ m^{-3} to ~1.6 MJ m^{-3}. However, the critical role that these β-sheet crystals play in silk's water-responsiveness is still unclear, and the challenge in controlling the formation of β-sheet crystals prevents practical applications.

We hypothesize that, during *B. mori* silk's WR actuation, β-sheet nanocrystal domains' high stiffness and strong interactions with adjacent amorphous domains facilitate the transfer of energy from the hygroscopic amorphous regions resulting in macroscale deformation. Based on this hypothesis, we sought to engineer a system that could enhance silk's water-responsiveness via the addition of stiff nanoparticle additives, mimicking the role of dispersed β-sheet nanocrystals. Owing to the high rigidity[12], and strong surface interactions between silica and silk proteins[13,14], this study applies silica nanoparticle as an additive to tune silk's WR behaviors. To test this composite system, silica nanoparticles of 5-15 nm (Sigma-Aldrich) are chosen as additives to mimic stiff crystal domains whose size ranges from 2-20 nm[11,15] in the silk.

The regenerated silk fibroin aqueous solution was first prepared by following protocols defined in Park et al[9]. Briefly, raw *B. mori* silk cocoons (TTSAM, Amazon) are cut into small fragments. Subsequently, the fragments are boiled in 0.02 M of aqueous sodium carbonate (Sigma-Aldrich) solution for 30 min and rinsed in cool ultrapure water to remove sericin and other impurities. The remaining silk fibroin was dissolved in 9.3 M aqueous LiBr solution with a ratio of 0.25 g silk to 1 mL LiBr at 60 °C for 2 h. The dissolved silk fibroin is then dialyzed in ultrapure water using regenerated cellulose dialysis tubing (molecular weight cut-off is 3,500 Daltons, Fisherbrand), and centrifuged at 6973 G for 20 min. The regenerated silk solution's yield a concentration of 5% to 8% (wt%).

The composite material is then made by adding untreated silica nanoparticles from suspensions (50 mg/mL) to the regenerated silk aqueous solution. The two-component system is ultrasonicated for 2-3 seconds (UP100H, Hielscher Ultrasonics) to form silk/silica-nanoparticles (SFSiNP) composite suspensions. ~6 µm thick solid SFSiNP composites with different solid silica nanoparticles concentrations (0 vol%, SFSiNP 0; 17 vol%, SFSiNP 17; 29 vol%, SFSiNP 29; 38 vol%, SFSiNP 38; 44

a. *Department of Chemical Engineering, The City College of New York, 160 Convent Avenue, New York, NY 10031, USA*

b. *Advanced Science Research Center (ASRC) at the Graduate Center, City University of New York, 85 St. Nicholas Terrace, New York, NY 10031, USA*

c. *Ph.D. Program in Chemistry, The Graduate Center of the City University of New York, 365 Fifth Avenue, New York, NY 10016 USA*

d. *Department of Physics at The City College of New York, City University of New York, 160 Convent Avenue, New York, NY 10031, USA*

e. *Ph.D. Program in Physics, The Graduate Center of the City University of New York, 365 Fifth Avenue, New York, NY 10016 USA*

Email: tu@ccny.cuny.edu, xchen@gc.cuny.edu

COMMUNICATION   **Soft Matter**

vol%, SFSiNP 44; and 50 vol%, SFSiNP 50) are created by depositing SFSiNP suspensions on 25 μm thick polyimide films (CAPLINQ), which were pre-cut into 3 mm x 6 mm pieces and oxidized with plasma (M 1070 NanoClean, Fischione) for 30 sec.
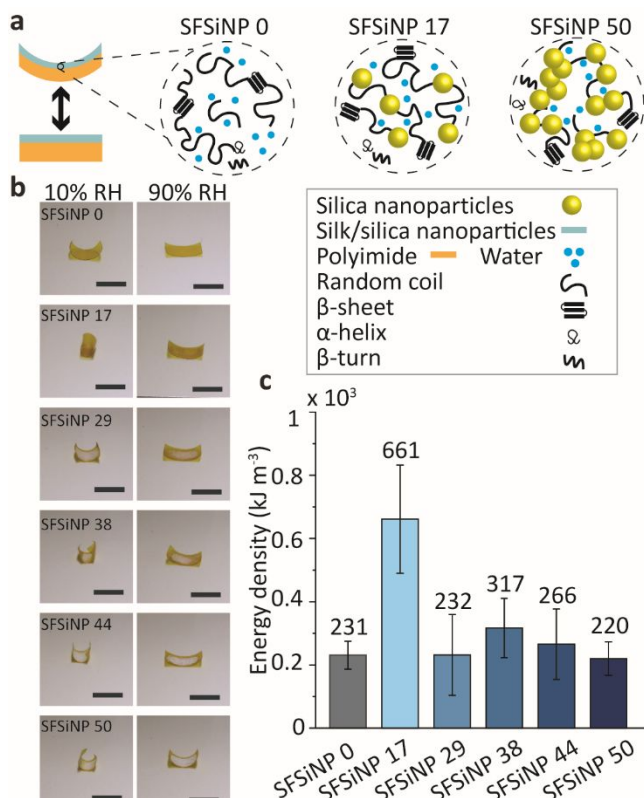

Fig. 1 (a) SFSiNP composites with various concentration of silica nanoparticles are deposited on polyimide substrates. (b) SFSiNP composites reversibly curve polyimide films when RH is alternated between 90% and 10%. Scale bar, 1 cm. (c) WR actuation energy density is calculated by estimating shape changes in wet (90%) and dry (10%) conditions. Errors bars represents standard deviations calculated from five different measurements.

After being dried at ambient condition overnight, a SFSiNP layer forms on top of polyimide films (**Fig. 1a**). The bilayer structures are then placed inside a humidity controlled champer, and films reversibly flex in response to changes in relative humidity (10% RH and 90% RH). We note that all films coated with SFSiNP show higher curvatures than those of films coated with silk, and the films with SFSiNP 17 show the highest WR performance (**Fig. 1b,** Fig. S1-2, and Movie S1).

Based on curvatures of these films, we estimated SFSiNP's WR actuation energy density by considering the elastic energy (U) stored in the curved bilayer structures, given by[1,9]:

$$U = \frac{(E_1 I_1 + E_2 I_2)L}{R^2} \quad (1)$$

where R is the radius of curved film, I_1 and I_2 are the area moment of inertia, and E_1 and E_2 (2.5 GPa) are Young's moduli of the SFSiNP and the polyimide substrate, respectively. E_1 can be calculated by using equation (2):

$$E_1 = \frac{1}{(f_{NPs}/E_{NPs} + (1 - f_{NPs})/E_{Silk})} \quad (2)$$

where f_{NPs} is the volume fraction of silica nanoparticles in SFSiNP, E_{NPs} is Young's modulus of silica nanoparticles (66.3 GPa), and E_{Silk} is Young's modulus of silk measured by AFM. Subsequently, the WR actuation energy density is calculated by dividing the elastic energy by the volume of the SFSiNP composites. Using this method, we found that all SFSiNP have higher energy densities (232 kJ m^{-3} for SFSiNP 29, 317 kJ m^{-3} for SFSiNP 38, 266 kJ m^{-3} for SFSiNP 44, and 220 kJ m^{-3} for SFSiNP 50) than that of the control silk (231 kJ m^{-3} for SFSiNP 0) (**Fig. 1c** and Fig. S3). Notably, the energy density of SFSiNP 17 reaches 661 kJ m^{-3}, exceeding that of natural spider silk (~500 kJ m^{-3})[8], indicating that silica nanoparticles can dramatically increase *B. mori* silk's WR performance.

To visualize the morphology of SFSiNP composites, scanning electron microscopy (SEM, Helios NanoLab 660) was used. As shown in **Fig. 2 a-b**, SFSiNP 17 shows a slightly increased surface roughness comparing to SFSiNP 0, indicating that silica nanoparticles are uniformly distributed within the silk matrix with a low degree of aggregation. However, SFSiNP with concentrations of silica nanoparticles higher than 29% show rough and porous structures due to the aggregation of silica nanoparticles (**Fig. 2 c-f**). These results show that the decreased WR actuation energy densities of SFSiNP 29-50 (**Fig. 1c**) correlate to the formation of these non-continuous, highly porous structures.
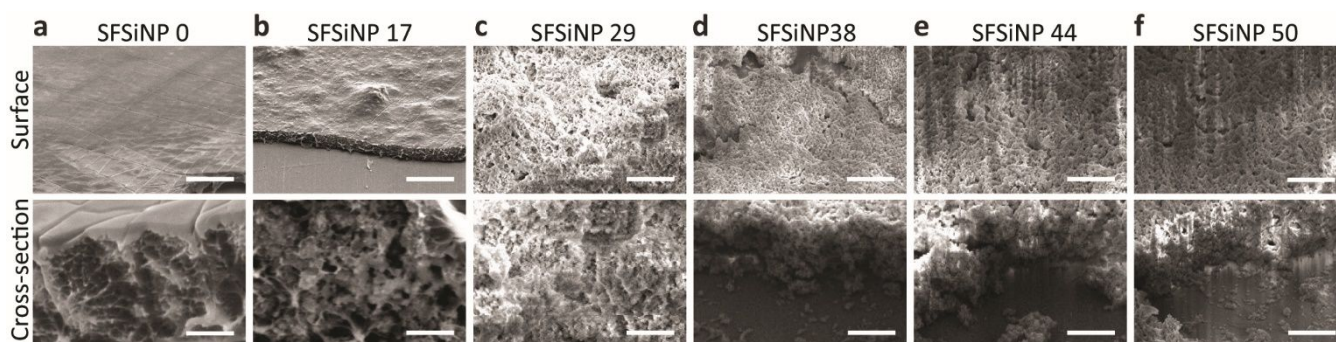

Fig. 2 SEM images of SFSiNP composites: surface and cross-section (a)-(f). Higher concentrations of silica nanoparticles result in high portion of aggregations. Scale bar, (a-b) 10 μm for surface images and 1 μm for cross-section images, (c-f) 10 μm.
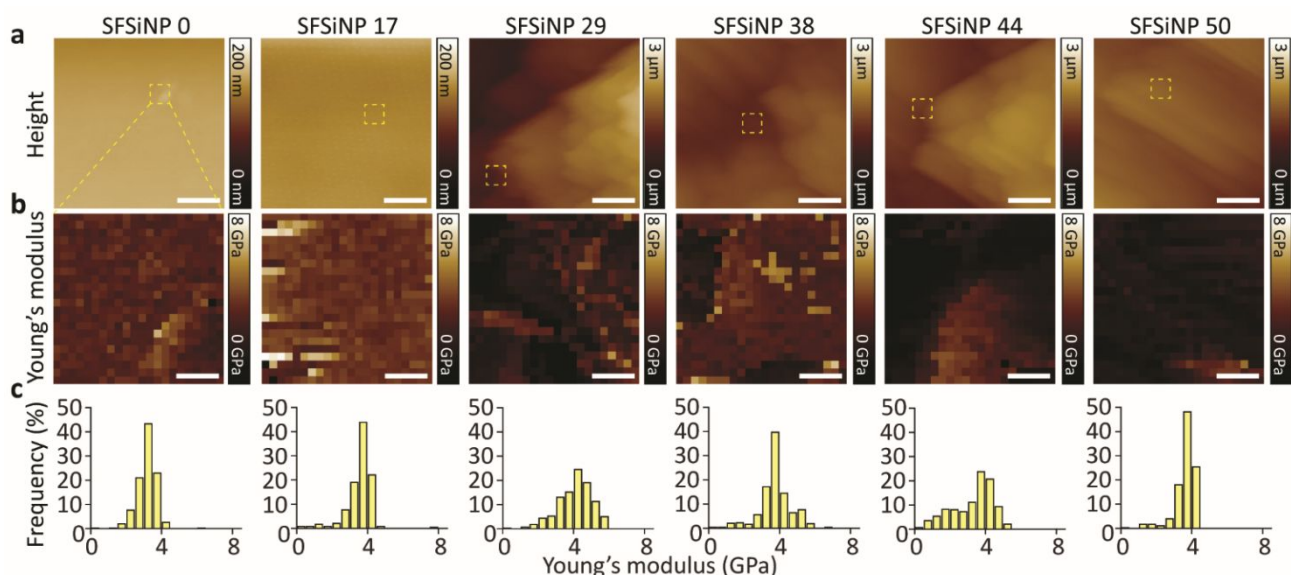
Fig. 3 (a) AFM topography maps show that silica nanoparticles can generally roughen silk's surface. Scale bar: 250 nm. (b) Young's modulus maps and (c) histograms show that silica nanoparticles slightly increase the stiffness of the silk. Young's modulus was measured by AFM peak force tapping and estimated by analysing peak force curves. Scale bar, 50 nm.

Atomic force microscopy (AFM, Multimode 8, Bruker) was used to further characterize SFSiNP's surface topology and quantify mechanical properties. As observed by SEM, the AFM topography maps show a higher surface roughness of SFSiNP 29-50 than SFSiNP 0 and 17 (**Fig. 3 a-b**). To measure SFSiNP's Young's modulus, AFM peak force tapping at ambient condition was used as described in Park et al[9]. Briefly, we used an AFM tip (RTESPA 525, Bruker) with a radius of ~50 nm and a spring constant of ~84 N m^{-1} to obtain force-separation curves, which were subsequently fitted by using a Hertz model:

$$F = \frac{4}{3(1-\nu^2)} E \sqrt{R} \delta^{3/2} \quad (3)$$

where F is force, E is Young's modulus, ν is Poisson's ratio (0.3 suggested by ref [16]), R is the tip radius, and δ is the indentation depth. A standard polystyrene sample with known modulus was also used to calibrate the measurement. Using this method, Young's modulus was analysed on flat regions within the same surface topography maps to eliminate the error caused by surface roughness (**Fig. 3b**). Histograms of the Young's modulus (**Fig. 3c**) show that silica nanoparticles only slightly increase the stiffness of the silk. SFSiNP 0 has a Young's modulus of 3.2 GPa (± 0.24), and SFSiNP 17-50 shows Young's moduli of 3.6 GPa (±

0.23), 4.1 GPa (± 0.22), 3.8 GPa (± 0.23), 3.3 GPa (± 0.24), and 3.7 GPa (± 0.23). These results suggest that silica nanoparticles do not significantly alter the silk microstructures, including its β-sheet crystallinity.

Attenuated total reflectance (ATR)-FTIR spectroscopy (Nicolet iS50 FTIR, Thermo Scientific) with a DTGS-KBr detector was used to evaluate the role of silica nanoparticles on *B. mori* silk's distribution of secondary structure. For each sample, spectra were collected between wavenumbers of 400-4,000 cm^{-1}, averaging 32 scans at a resolution of 4 cm^{-1}. As shown in **Fig. 4a**, the FTIR spectra reveals new peaks in amide I and II bands as a consequence of silica nanoparticles, but there is no clear peak shifting from random coil rich region (~1,645 cm^{-1}) to β-sheet rich region (~1,620 cm^{-1}) in the SFSiNP samples. To quantify silk's secondary structures, Amide I band (1,600-1,700 cm^{-1}) is deconvoluted (OriginPro 2018) based four representative peaks, including β-sheet (1620 cm^{-1}), random coil (1645 cm^{-1}), α-helix (1660 cm^{-1}), and β-turn (1678 cm^{-1}) suggested by ref[17], using Gaussian distributions. Based on the area of each sub peak, we estimated the relative secondary structural contents of *B. mori* silk in SFSiNP (**Fig. 4 b-c**).

This analysis shows that SiNPs 0's silk matrix consists of 21% (± 2.14) β-sheet content, 50% (± 1.55) random coil, 19% (± 2.59)
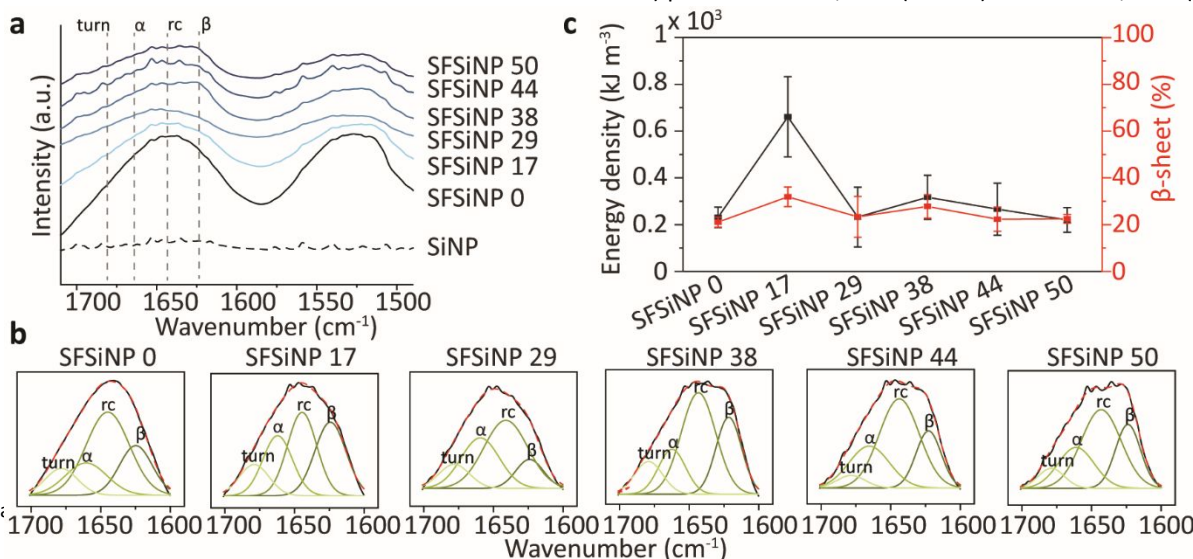

Fig. 4 (a) FTIR spectra shows the appearance of silica nanoparticle peaks compared to control silk. No notable peak shifting from random coil rich region to β-sheet rich region is observed. (b) The amide I bands of *B. mori* silk are deconvoluted into β-sheet (β, ≈1624 cm^{-1}), random coil (rc, ≈1647 cm^{-1}), α-helix (α, ≈1660 cm^{-1}), and β-turn (turn, ≈1679 cm^{-1}). (c) SFSiNP composites' WR energy densities and β-sheet contents. Errors bars represents standard deviations calculated from five different measurements.

α-helix, and 10% (± 2.38) β-turn, which agrees with distributions reported in previous studies[18]. While silk matrix of SFSiNP showed slightly higher β-sheet concentrations, 32% (± 5.26) for SFSiNP 17, 23% (± 8.73) for SFSiNP 29, 28% (± 5.02) for SFSiNP 38, 22% (± 5.16) for SFSiNP 44, and 22% (± 1.86) for SFSiNP 50, the changes in their secondary structures are not statistically significant. This result is consistent with the minimal change in Young's moduli as measured by AFM. Taken together, these results suggest that the increased WR energy densities of SFSiNP, especially the SFSiNP 17 sample, are not a consequence of silk's crystallinity but the silica nanoparticle. We also note that the increased surface roughness can result in shallower depths of penetration of the ATR method (0.5-2 µm), affecting standard deviation of the FTIR measurement.

Our results suggest that, similar to silk's β-sheet crystals, stiff silica nanoparticles can dramatically increase amorphous silk's water-responsiveness and reduce energy dissipation during hydration and dehydration processes. Notably, despite a lower β-sheet crystallinity of SFSiNP composites than that of spider silk (36-37%), SFSiNP still exhibit a higher WR energy density than that of spider silk (~500 kJ m^{-3})[19]. However, the silk with high silica nanoparticle concentrations, such as SFSiNP 29-50, shows a decreased WR energy density, which appears to be a consequence of the high degree of silica nanoparticles aggregation, preventing the deformation of amorphous silk and reducing the WR energy transfer efficiency. This hypothesis can also explain our previously observed decrease in WR energy density of *B. mori* silk with a crystallinity higher than ~58%[9].

Conclusions

We demonstrated that the regenerated *B. mori* silk's water-responsiveness can be dramatically enhanced by simply adding silica nanoparticles, without significant formation of β-sheet crystals. This is due to the homogeneously distributed stiff silica nanoparticle domains surrounded by the hygroscopic amorphous continuous domains contributing to reduce energy dissipation during WR deformation. This work sheds light on the potential approach of using silk fibroin matrix with the stiff nanosized structures to develop a low cost but simple and high-energy WR actuator.

Author contribution

X.C., R.S.T., and Y.J. conceived and initiated the project. Y.J. prepared the silk and SFSiNP. S.S.G. performed FTIR measurements. T.D.L performed the AFM experiment. Y.J. analysed the data. Y.J., R.S.T, and X.C. wrote the paper. All authors provide critical feedback and contributed to the final manuscript.

Conflicts of interest

There are no conflicts to declare.

References

1. Y. Park and X. Chen, *J. Mater. Chem. A*, 2020, **8**, 15227–15244.
2. B. Shin, J. Ha, M. Lee, K. Park, G. H. Park, T. H. Choi, K.-J. Cho, and H.-Y. Kim, *Sci. Robot.*, 2018, **3**, 1–9.
3. K. Zhang, A. Geissler, M. Standhardt, S. Mehlhase, M. Gallei, L. Chen and C. M. Thiele, *Sci. Rep.*, 2015, **5**, 1–12.
4. A. Menges and S. Reichert, *Archit. Des.*, 2012, **82**, 52–59.
5. C. Dawson, J. F. V. Vincent and A.-M. Rocca, *Nature*, 1997, **390**, 668.
6. R. Elbaum, L. Zaltzman, I. Burgert and P. Fratzl, *Science*, 2007, **316**, 884–886.
7. X. Chen, L. Mahadevan, A. Driks and O. Sahin, *Nat. Nanotechnol.*, 2014, **9**, 137–141.
8. I. Agnarsson, A. Dhinojwala, V. Sahni and T. A. Blackledge, *J. Exp. Biol.*, 2009, **212**, 1990–1994.
9. Y. Park, Y. Jung, T.-D. Li, J. Lao, R. S. Tu and X. Chen, *Macromol. Rapid Commun.*, 2020, **41**, 1–6.
10. R. Elbaum, S. Gorb and P. Fratzl, *J. Struct. Biol.*, 2008, **164**, 101–107.
11. S. Keten, Z. Xu, B. Ihle and M. J. Buehler, *Nat. Mater.*, 2010, **9**, 359–367.
12. M. S. Islam, R. Masoodi and H. Rostami, *J. Nanosci.*, 2013, **2013**, 275037.
13. L. Shen, L. Guo, S. Chen, A. Wei, A. Osaka and W. Chen, *J. Non. Cryst. Solids*, 2019, **522**, 119557.
14. J. Wang, S. Yang, C. Li, Y. Miao, L. Zhu, C. Mao and M. Yang, *ACS Appl. Mater. Interfaces*, 2017, **9**, 22259–22267.
15. D. Li, Q. Wang, C. Xu, Y. Cheng, Y.-W. Zhang and B. Ji, *Nano Lett.*, 2020, **20**, 8516-5823.
16. H. Sun and B. Marelli, *Nat. Commun.*, 2020, **11**, 351.
17. N. Qin, S. Zhang, J. Jiang, S. G. Corder, Z. Qian, Z. Zhou, W. Lee, K. Liu, X. Wang, X. Li, Z. Shi, Y. Mao, H. A. Bechtel, M. C. Martin, X. Xia, B. Marelli, D. L. Kaplan, F. G. Omenetto, M. Liu and T. H. Tao, *Nat. Commun.*, 2016, **7**, 1–8.
18. B. D. Lawrence, F. Omenetto, K. Chui and D. L. Kaplan, *J. Mater. Sci.*, 2008, **43**, 6967–6985.
19. T. Lefèvre, M.-E. Rousseau and M. Pézolet, *Biophys. J.*, 2007, **92**, 2885–2895.